Computational Analysis of Ice Accretion Roughness on Aerodynamic Performance

Victor Hernandez*, Anicyah Moreira†, Akash Saravanan.‡, David Rondon§, Alonso Arregui Martinez¶, Daniel Gomez‖, Reagan Ruben** and Dr. Suhas Jain††
College of Engineering, Georgia Institute of Technology, Atlanta, GA 30332, USA

This paper will explore the results simulations performed on a two-dimensional and three-dimensional 20° swept wing NACA0012 with ice profiles generated by LEWICE, spanning a range of angles of attack 0° to 15° to capture changes in lift, drag, and pressure coefficient distributions. Flow visualizations reveal the onset and progression of flow separation associated with ice-induced surface roughness, in agreement with prior experimental and numerical icing studies. These findings aim to provide insight into the mechanisms by which ice reduces aerodynamic efficiency and highlight parameters most critical for performance loss. Ultimately, this work supports the development of improved de-icing and anti-icing technologies, contributing to safer and more efficient cold-weather aviation operations and the predictive capability of ice accretion simulation software coupled with CFD analysis.*

I. Introduction

Ice accretion occurs when supercooled water droplets encountered at altitude freeze upon impact with an aircraft surface, forming rough, irregular deposits that disrupt the airfoil contour. The resulting surface roughness increases drag, reduces lift, alters pressure distributions, and promotes premature boundary-layer separation, potentially leading to stall or loss of control [1].

Aircraft icing has posed a persistent challenge since the early 20th century, with documented incidents in the late 1920s reporting sudden lift loss and degraded controllability [1]. Its severity became particularly evident during World War II, when high-altitude military operations exposed aircraft to prolonged icing conditions, resulting in unexplained performance losses and mission aborts. Unlike combat damage, icing was unpredictable, often undetected until aerodynamic degradation occurred, and capable of producing highly nonlinear flow effects. These risks motivated systematic research efforts, including the establishment of the NACA Icing Research Tunnel in 1944 to replicate atmospheric icing conditions and quantify aerodynamic penalties [2].

Although experimental campaigns have significantly advanced understanding and certification standards, particularly following accidents such as USAir Flight 405 and American Eagle Flight 4184 in the 1980s [3], wind tunnel and flight testing remain costly and limited in scope. Consequently, Computational Fluid Dynamics (CFD) has emerged as a complementary tool for analyzing ice-induced flow modifications, boundary-layer behavior, and wake dynamics.

II. Methodology

A. Computational Framework

A Reynolds-Averaged Navier Stokes (RANS) framework was employed across the computational domain to model turbulent flow behavior under high-Reynolds-numbers. For realistic icing conditions, the thin turbulent boundary layers along the airfoil surface exhibit steep velocity gradients that would require prohibitively-fine grids if resolved

*Undergraduate, Aerospace Engineering, Student Member 1810998
†Undergraduate, Aerospace Engineering, Student Member 1922300
‡Undergraduate, Aerospace Engineering, Student Member 1924078
§Undergraduate, Mechanical Engineering, Student Member 1924185
¶Undergraduate, Aerospace Engineering, Student Member 1744177
‖Undergraduate, Aerospace Engineering, Student Member 1924087
**Undergraduate, Biomedical Engineering, Student Member 1923970
††Faculty Advisor, Department of Mechanical Engineering

*For an overview of the challenges associated with aircraft icing and its impact on performance, see Gent, R. W., Dart, N. P., and Cansdale, J. T. (2000). *Aircraft Icing*. Philosophical Transactions of the Royal Society of London A, 358(1776), 2873–2911.

directly. Therefore, a RANS approach provides an appropriate balance between computational efficiency and predictive capability to satisfy such conditions. Specifically, the k-ω SST (Shear Stress Transport) turbulence model [4] was selected to capture mean flow properties and modeled turbulent stresses with reduced computational expense. The k-ω SST formulation is well-suited to address flows involving adverse pressure gradients and separation phenomena in turbulent flow, both are crucial considerations when considering surface roughness changes due to ice accretion.

B. Governing Equations

In the RANS region, the governing equations are derived from the compressible Navier–Stokes equations, with a focus on mass continuity and momentum conservation, and can be expressed as:

1. Conservation of Mass:

$$\frac{\partial \rho}{\partial t} + \nabla \cdot (\rho \mathbf{u}) = 0 \tag{1}$$

2. Conservation of Momentum:

$$\frac{\partial \rho \mathbf{u}}{\partial t} + \nabla \cdot (\rho \mathbf{u} \otimes \mathbf{u}) = -\nabla p + \nabla \cdot \tau \tag{2}$$

3. Conservation of Energy:

$$\frac{\partial \rho E}{\partial t} + \nabla \cdot (\mathbf{u}(\rho E + p)) = \nabla \cdot (k_{th} \nabla T + (\tau \cdot \mathbf{u})) \tag{3}$$

C. Boundary Conditions

1. Two-Dimensional Conditions

For the 2-D simulations, the freestream velocity was specified as $\mathbf{U}_\infty$ = 104 m/s in the streamwise direction, with a freestream static pressure of $\mathbf{P}_\infty$ = 92,321 Pa, turbulent kinetic energy of $\mathbf{k}_\infty$ = 37 m^2/s^2, and specific dissipation rate of ω_∞ = 158 s^{-1}. The pressure field was initialized to a uniform reference value of zero across the domain.

At the inlet boundary, U, k, and ω were fixed to their prescribed freestream values, while pressure was extrapolated from the interior. At the outlet, pressure was fixed to the reference value, and U, k, and ω were extrapolated from the interior to allow fully developed flow condition The airfoil surface was modeled as a no-slip moving wall to account for the dynamic mesh motion. The top and bottom far-field boundaries were treated as slip walls, representing a frictionless external flow environment. The front and back were defined to enforce a two-dimensional formulation of the domain.

2. Three-Dimensional Conditions

For the 3-D simulations, the freestream velocity was specified as $\mathbf{U}_\infty$ = 63 m/s in the streamwise direction, with a freestream static pressure of $\mathbf{P}_\infty$ = 92,321 Pa, turbulent kinetic energy of $\mathbf{k}_\infty$ = 37 m^2/s^2, and specific dissipation rate of ω_∞ = 158 s^{-1}. The pressure field was initialized to a uniform reference value of zero across the domain.

At the inlet boundary, U, k, and ω were fixed to their prescribed freestream values, while the pressure was extrapolated from the interior. At the outlet, pressure was fixed to the reference value, while U, k, and ω were extrapolated from the interior to allow fully developed flow conditions. The airfoil surface, including both upper and lower surfaces, was modeled as a stationary no-slip wall. All remaining outer boundaries were treated as slip walls, representing a frictionless far-field enclosure appropriate for external three-dimensional aerodynamic simulations.

III. Flow Conditions

Below are the different flow conditions that our airfoil experienced. Due to validation constraints, the two-dimensional and the three-dimensional cases had to be run under different conditions to maintain simulation integrity. However, because neither flow exceeds a Mach number of 0.3, compressibility effects can be ignored and the calculation for the coefficient of pressure remains the same.

Table 1 Freestream and near-wall resolution parameters for CFD cases

Case	Velocity	Mach	Re_c	u_τ	Target y^+	Δy (m)
2D Clean/Iced	104 m/s	0.30	3.8×10^6	4.29	1	3.4×10^{-6}
3D Clean/Iced	63 m/s	0.18	2.3×10^6	2.76	1	5.3×10^{-6}

IV. Ice Geometry Generation (LEWICE)

The LEWICE icing software was utilized to generate ice accretion profiles for both the two- and three-dimensional simulation cases. Identical icing conditions were applied in LEWICE to replicate the validation case corresponding to the run ID presented in Figure 9 of Ref. [5]. Both 2D and 3D airfoil configurations were evaluated to ensure consistency between the generated ice shapes and the documented experimental data.

Table 2 Icing conditions for the NACA 0012 two-dimensional validation case from Ref. [5]

Parameter	Value
Accretion Time (s)	360
Angle of Attack, α (°)	4
Chord (m)	0.5334
Airspeed (m/s)	67.05
Atmospheric Pressure (Pa)	101,300
Liquid Water Content (g/m^3)	1.0
Median Volumetric Diameter (μm)	20
Temperature (C°)	−5.6

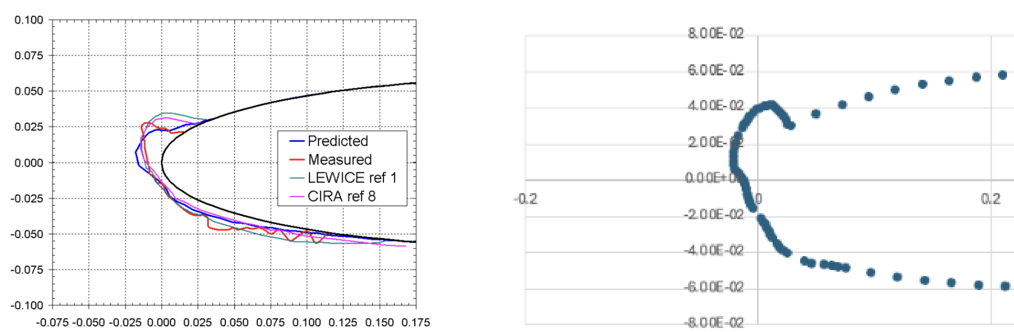

(a) Ice profile at -5.6°C and 1.00g/m^3 for the two-dimensional validation case from Ref. [5]

(b) LEWICE-generated ice profile

Fig. 1 Comparison between experimental validation data and LEWICE-generated ice profile under identical icing conditions

The comparison shown in figures above demonstrates strong geometric agreement between the published validation case and the LEWICE-generated ice profile under identical atmospheric and flow conditions. The location and shape of the primary leading-edge horn are captured with good fidelity, and the overall accretion thickness trends closely follow the documented experimental results. Minor discrepancies in downstream ice growth are attributed to modeling assumptions inherent in the thermodynamic formulation and numerical discretization. Based on this level of agreement, the generated ice geometry is considered sufficiently accurate to serve as a validation case for the following CFD simulations.

V. Ice Accretion and Multiphase Modeling

1. Droplet Flow Field Model

Ice accretion occurs when supercooled droplets, commonly encountered at high altitudes within cirrus or mixed-phase cloud environments, freeze upon impact with an aircraft surface. Accurate simulation of ice accretion therefore requires that the LEWICE solver incorporate a robust model capable of resolving dispersed droplet transport and surface impingement dynamics.

A Lagrangian particle tracking approach was adopted to capture the dynamics of supercooled droplet–air interactions within the turbulent compressible flow field. Using this method, individual droplets are tracked through the carrier-phase velocity field by integrating their equations of motion, accounting for drag and gravitational forces. This method enables accurate prediction of droplet trajectories and impingement locations, which are used to compute local collection efficiency.
[†]

The motion of each droplet is governed by Newton's second law, accounting primarily for aerodynamic drag and gravitational forces. Neglecting higher-order effects such as added mass and history forces, the droplet momentum equation is expressed as:

$$m_p \frac{d\mathbf{u}_p}{dt} = \frac{1}{2} C_d \rho \left| \mathbf{u} - \mathbf{u}_p \right| \left(\mathbf{u} - \mathbf{u}_p \right) A_p + m_p \mathbf{g}, \tag{4}$$

where m_p is the droplet mass, $\mathbf{u}_p$ is the droplet velocity, $\mathbf{u}$ is the local air velocity obtained from the flow solver, C_d is the drag coefficient, ρ is the air density, A_p is the projected droplet area, and $\mathbf{g}$ is gravitational acceleration. The droplet position is updated from

$$\frac{d\mathbf{x}_p}{dt} = \mathbf{u}_p. \tag{5}$$

Droplet impingement on the airfoil geometry is determined by detecting trajectory intersections with the surface. From the mass flux of droplets striking each surface location, the local collection efficiency is computed. This collection efficiency serves as the mass input to the subsequent thermodynamic ice accretion model.

The droplet solver operates in conjunction with the airflow solution, with droplet trajectories computed using the steady carrier-phase velocity field. Because the liquid water content in atmospheric icing conditions is typically low, the dispersed phase is assumed to have negligible influence on the airflow, and droplet–droplet interactions are neglected.

VI. Geometry & Meshing

The process of meshing the airfoils was of great importance, since we needed meshes with such a resolution so as to clearly capture the detail of the ice accretion. The process can be broken down into two parts: 2-D and 3-D.

1. 2-Dimensional Meshing

Because these experiments were performed with existing airfoils, the *Blender* application was used to import the coordinates of the NACA 0012 airfoil for physical manipulation. Once the vertices were in position and joined, a face was created, extruded and oriented it to our liking. Since the mesh was two-dimensional, the length of the initial extrusion is irrelevant. Finally, the geometry was exported as an STL file so it could be utilized in OpenFOAM to mesh the new airfoil. We began by editing the blockMeshDict file inside of the system folder. The vertices were defined as thin (0.2 meters and 1 cell thick) blocks which surrounded the airfoil with the front and back faces of type symmetryPlane, as the goal was to have the solver mirror the entire structure since it is a two-dimensional case; this approach served as an efficient way to make the simulations less expensive computationally .[‡]

For snappyHexMeshDict, the castellatedMesh, snap, and addLayers features were set to be true. The following features carved the mesh from the surrounding box (castellatedMesh), smooth the edges of the mesh (snap) , and added a specified number of layers to ensure accuracy near the surface of our airfoil. Lastly, the refinementBox feature was utilized on the entire airfoil to capture as much detail as possible. For the 2D cases, it was necessary to include

[†] Goldstein, R. J. (1998). *Droplet Dynamics in Airflow*. Journal of Aerosol Science, 29(5), 623–644.
[‡] Anderson, J. D. (1995). *Computational Fluid Dynamics: The Basics with Applications*. McGraw-Hill.

extrudeMesh, which was responsible for ensuring that only 1 cell makes up the thickness of the mesh. The following dictionaries were ran: blockMesh, snappyHexMesh, and extrudeMesh to obtain these results:

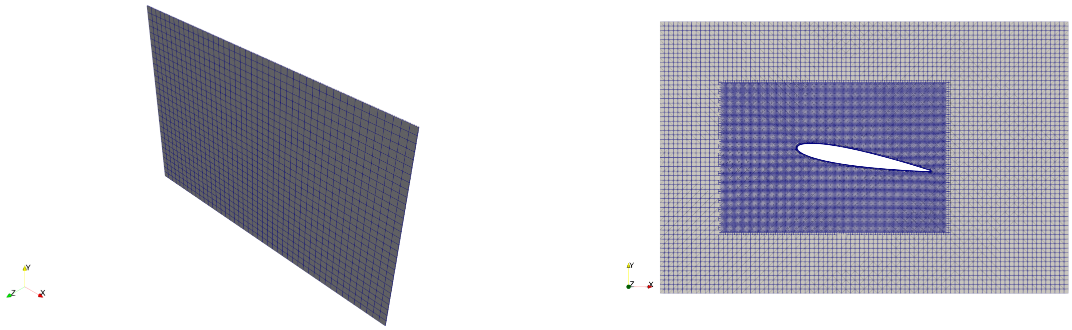

(a) After execution of blockMesh

(b) After execution of snappyHexMesh and extrudeMesh

Fig. 2 Results of blockMesh and snappyHexMesh for the 2D case

*2. **3-Dimensional Meshing***

The 3D process is very similar to the previous but with a few key differences. The mesh was extruded to exactly twice its chord length. This time, blockMeshDict was used to enclose the entire airfoil with several cells in all three axes, and only type patch surfaces were defined. Then a new dictionary, surfaceFeatureExtractDict, was defined. It was used to extract any sharp edges and feature lines from the 30 STL file prior to meshing to ensure that critical geometric details are preserved in the final mesh. Lastly, snappyHexMeshDict was then defined similarly: castellatedMesh, snap, and addLayers were all set to true, but the refinement box was now defined as an area enclosing the airfoil but still within the bigger box parameters to greatly save on computing time while still retaining an accurate simulation. After all three commands were executed, the following results were obtained:

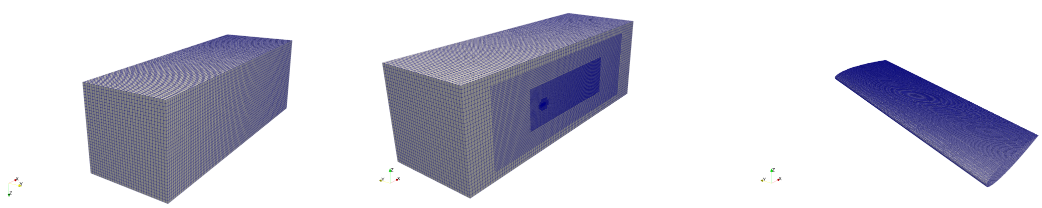

(a) Base mesh generated using blockMesh

(b) Surface refinement using surfaceFeatureExtract and snappyHexMesh

(c) Close-up view of the refined airfoil mesh

Fig. 3 Mesh generation process for the three-dimensional case: (top left) initial structured mesh created with blockMesh; (top right) surface-conforming mesh after refinement with snappyHexMesh; (bottom) detailed view of the refined mesh near the airfoil surface.

The meshes shown in Figures 2 and 3 illustrate the progressive refinement process from the initial background grid to the final body-fitted configuration. In both the two- and three-dimensional cases, the initial blockMesh establishes a structured outer domain that ensures adequate far-field resolution and minimizes boundary interference effects. Following refinement and snapping, snappyHexMesh conforms the grid to the airfoil geometry, resolving the leading-edge curvature and any ice accretion features with significantly improved fidelity. The addition of prism layers near the surface enhances boundary layer resolution, which is critical for accurately predicting wall shear stress and pressure gradients. This process is essential to maintain computational efficiency without sacrificing solution accuracy. [§]

[§]For additional details on meshing strategies in ice accretion simulations, see Anderson (1995) and related literature.

VII. Data Results

As mentioned previously, both two-dimensional and three-dimensional simulations were executed across different α values for both iced and non-iced airfoils. The simulations provided .foam files which can be opened in the *Paraview* application. Additionally, they carry aerodynamic coefficients data that can display time-stepped flow visualizations in *Paraview* as well. The post-processing results were compared with available experimental data and validation data from previous icing models [6] to validate OpenFOAM's capability in predicting ice-induced impacts on the aerodynamic performance. The data acquired from the simulation was plotted as the C_p, vs x/c for pressure distribution analysis purposes.

A. 2D Results

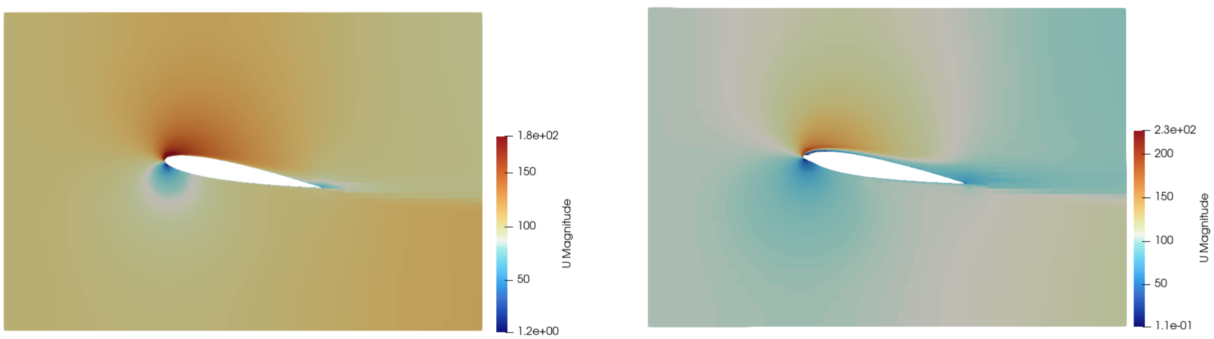

(a) Non-iced slice of 2D flow velocity at α = 10°

(b) Iced slice of 2D flow velocity at α = 10°

Fig. 4 Flow velocity comparison between 2D LEWICE-generated iced and non-iced NACA0012 airfoils

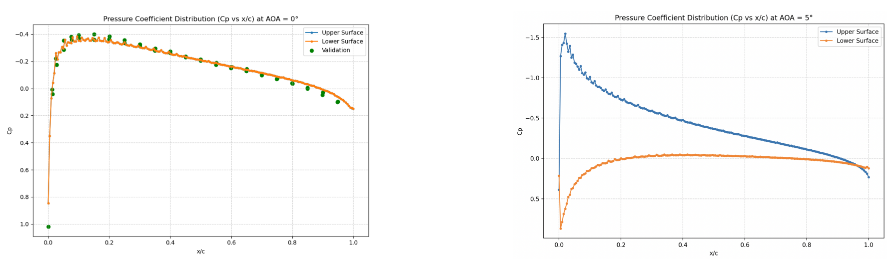

(a) C_p vs x/c for the non-iced 2D airfoil at α = 0°

(b) C_p vs x/c for the non-iced 2D airfoil at α = 5°

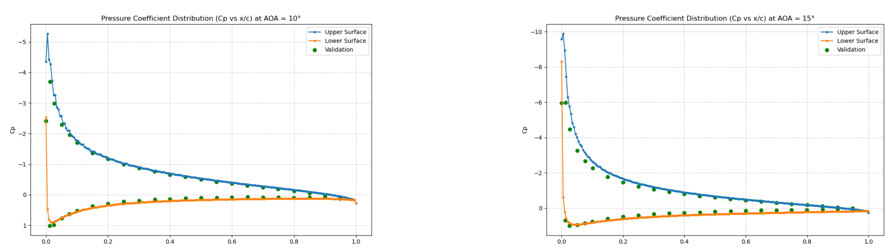

(c) C_p vs x/c for the non-iced 2D airfoil at α = 10°

(d) C_p vs x/c for the non-iced 2D airfoil at α = 15°

Fig. 5 C_p vs x/c for the non-iced 2D airfoils

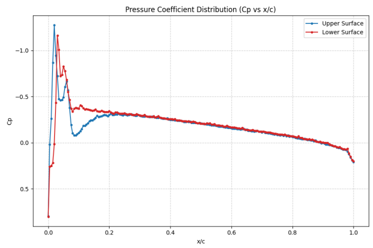

(a) C_p vs x/c for the iced 2D airfoil at α = 0

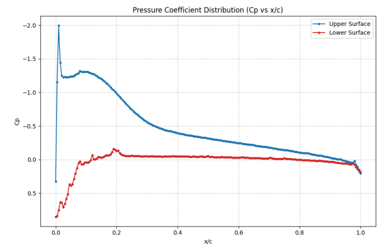

(b) C_p vs x/c for the iced 2D airfoil at α = 5

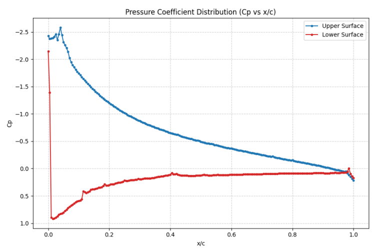

(c) C_p vs x/c for the iced 2D airfoil at α = 10

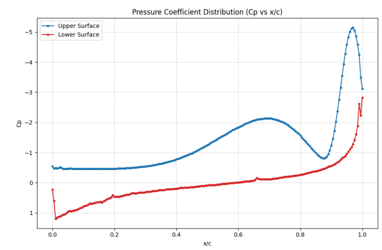

(d) C_p vs x/c for the iced 2D airfoil at α = 15

Fig. 6 C_p vs x/c for the iced 2D airfoilsl

B. 3D Results

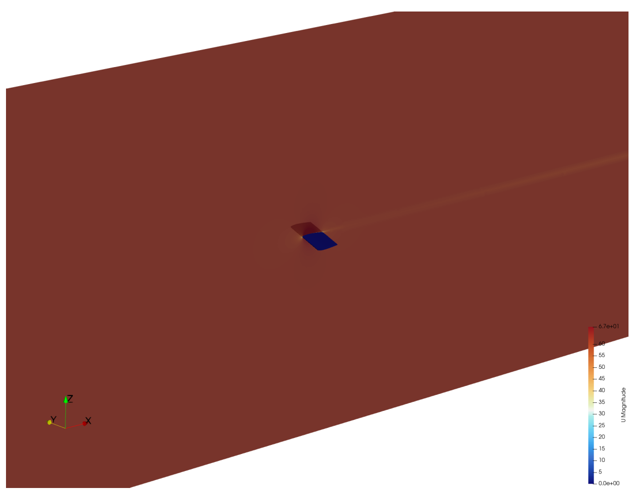

(a) Sliced 3D airfoil at $\alpha = 0°$

Fig. 7 Slice of 3D flow velocity for AOA = $0°$

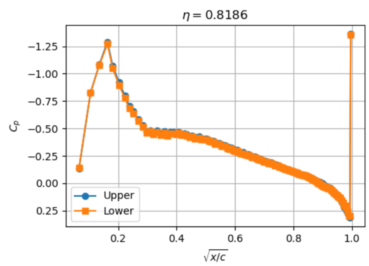

(a) C$_p$ vs $\sqrt{x/c}$ for the non-iced 3D wing at α = 0°and η = 0.8186

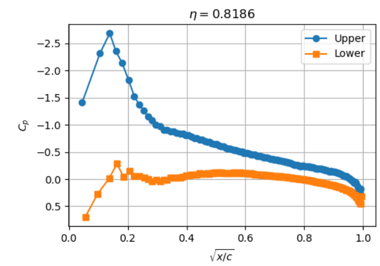

(b) C$_p$ vs $\sqrt{x/c}$ for the non-iced 3D wing at α = 5° and η = 0.8186

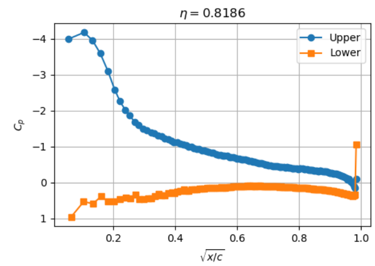

(c) C$_p$ vs $\sqrt{x/c}$ for the non-iced 3D wing at α = 10° and η = 0.8186

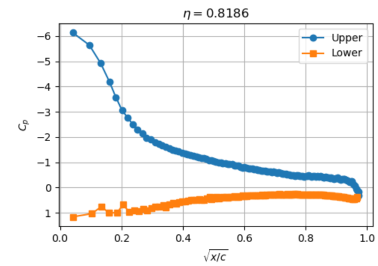

(d) C$_p$ vs $\sqrt{x/c}$ for the non-iced 3D wing at α = 15° and η = 0.8186

Fig. 8 C$_p$ vs $\sqrt{x/c}$ for the non-iced 3D wing at η = 0.8186

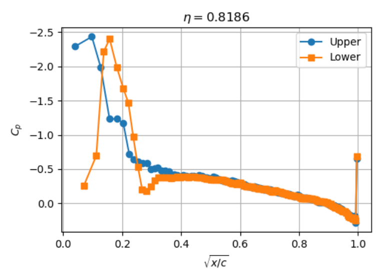

(a) C$_p$ vs $\sqrt{x/c}$ for the iced 3D wing at α = 0°and η = 0.8186

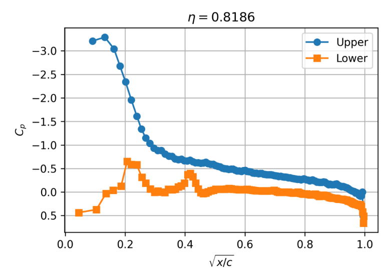

(b) C$_p$ vs $\sqrt{x/c}$ for the iced 3D wing at α = 5°and η = 0.8186

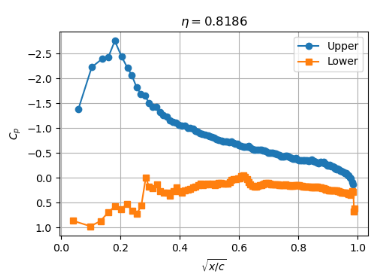

(c) C$_p$ vs $\sqrt{x/c}$ for the iced 3D wing at α = 10°and η = 0.8186

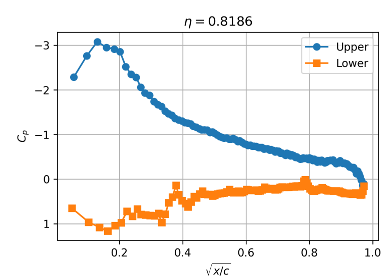

(d) C$_p$ vs $\sqrt{x/c}$ for the iced 3D wing at α = 15°and η = 0.8186

Fig. 9 C$_p$ vs $\sqrt{x/c}$ for the iced 3D wing at η = 0.8186

VIII. Conclusion

In figure 4, distinct behaviors can be observed in the flow velocity ($t = 0.024s$) after entering in contact with both airfoils. In (a), the flow rapidly streamlines across the upper surface of the airfoil, whereas in (b) after the entering in contact with the ice, the flow slows down immediately. This change in flow velocity impacts the graphs inversely by Bernoulli's equation. Naturally, higher velocity implies lower pressure distributions and vice-versa and stable flight conditions require negative C_p values on the upper surface and positive C_p on lower surface of the wing. This general behavior is predictable and can be observed in figures 5 and 8 as α increases until the airfoil stalls, throughout the chord length. When icing conditions are ideal and ice growth occurs on the airfoil, it disturbs not only the oncoming flow velocity, but the pressure distributions on both surfaces, as can be seen in figures 6 and 9. These disturbances can make aerodynamic performance unstable, drastically unpredictable, and force the predictable behaviors such as $C_{L,max}$ and consequently stall to occur at lower α due to the ice's capability of reducing flow velocity and decimate pressure distributions.

This research highlights the risk that ice accretion presents to modern aviation and emphasizes the need of improved de-icing and anti-icing technologies as preventative measures to protect the millions who board flights daily from irreparable damage.[¶]

IX. Acknowledgements

The authors acknowledge the Virtually Integrated Projects (VIP) Program at the Georgia Institute of Technology, for providing the collaborative framework that supported this work. The authors also extend their appreciation to Dr. Suhas Jain, advisor of the Exascale Computational Fluid Dynamics VIP, for his mentorship throughout the project. The authors also acknowledge Martha Mwangi for her contributions to the post-processing and analysis efforts.

This research was supported in part through research cyberinfrastructure resources and services, including the AI Makerspace of the College of Engineering, provided by the Partnership for an Advanced Computing Environment (PACE) at the Georgia Institute of Technology, Atlanta, Georgia, USA. (RRID:SCR_027619)

[¶]For further reading on CFD-based prediction models for aircraft icing, see Gent et al. (2000).

References

[1] Masafumi, Y., and Others, “A Review on the Current Status of Icing Physics and Mitigation in Aviation,” Tech. Rep. 1, Departnment of Aerospace and Mechanical Engineering, University of Notre Dame, 2021.

[2] Bragg, M. B., Broeren, A. P., and Paull, A., “Aerodynamic Effects of Ice Accretion on Airfoils,” *Journal of Fluids Engineering*, Vol. 118, No. 4, 1996, pp. 660–667. https://doi.org/10.1115/1.2817780.

[3] National Transportation Safety Board, “Aircraft Accident Report: American Eagle Flight 4184,” Tech. Rep. NTSB/AAR-96/01, National Transportation Safety Board, 1996.

[4] Menter, F. R., “Two-Equation Eddy-Viscosity Turbulence Models for Engineering Applications,” *AIAA Journal*, Vol. 32, No. 8, 1994, pp. 1598–1605. https://doi.org/10.2514/3.12149.

[5] Fortin, L. J., G., and Beisswenger, A., “Prediction of Ice Shapes on NACA0012 2D Airfoil,,” Tech. Rep. 2003-01-2154, SAE, 2003. Technical Report.

[6] Group, T. M. B. W., “2D NACA 0012 Airfoil Validation.” Tech. rep., AIAA,TMBWG and FDTC, 2016. Technical Resource website.

[7] Anderson, J. D., *Computational Fluid Dynamics: The Basics with Applications*, McGraw-Hill, New York, 1995.

[8] Gent, R. W., Dart, N. P., and Cansdale, J. T., “Aircraft Icing,” *Philosophical Transactions of the Royal Society of London A*, Vol. 358, No. 1776, 2000, pp. 2873–2911. https://doi.org/10.1098/rsta.2000.0689.

[9] Goldstein, R. J., “Droplet Dynamics in Airflow,” *Journal of Aerosol Science*, Vol. 29, No. 5, 1998, pp. 623–644.

[10] Leary, W. M., *We Freeze Planes: A NASA Icing Research Tunnel*, NASA History Office, Washington, DC, 2002.

[11] Luhar, A. K., and Nepf, H. M., “Effect of Roughness on Flow in Open Channels,” *Journal of Hydraulic Engineering*, Vol. 133, No. 8, 2007, pp. 901–912.

[12] Messinger, D. W., “A Mathematical Model for Aircraft Icing Conditions,” *Journal of Aircraft*, Vol. 24, No. 12, 1987, pp. 1041–1046.

[13] NASA, “Icing Research Tunnel: Empirical Data and Performance Studies,” Tech. Rep. NASA/TM–2006-214123, NASA, 2006.

[14] Perkins, C. D., and Hage, R. E., “Aircraft Icing and Aerodynamic Performance,” *Journal of the Aeronautical Sciences*, Vol. 4, No. 3, 1938, pp. 123–130. https://doi.org/10.2514/3.11368.

[15] Spaart, S., and Others, “A Detached Eddy Simulation Approach for High-Reynolds Number Flows,” Tech. rep., 1997. Technical Report or Conference Paper, details unknown.

[16] Broeren, A., and Others, “Aerodynamic Simulation of Ice Accretion on Airfoils,,” Tech. Rep. NASA/TP—2011-216929, NASA., 2011. Technical Report.

[17] Feng, Y., “Lift/Drag Characteristics of Different Ice Accretion Airfoil,”,” Tech. rep., IOP, 2019. Technical Report.

[18] MacArthur, C., “Numerical Simulation of Airfoil Ice Accretion,” Tech. rep., AIAA, 2012. Technical Report, https://arc.aiaa.org/doi/abs/10.2514/6.1983-112.